

Optimizing the dynamical preparation of quantum spin lakes on the ruby lattice

DinhDuy Vu,^{1,2,*} Dominik S. Kufel,^{1,2,*} Jack Kemp,^{1,2,3}
Lode Pollet,^{4,5} Chris R. Laumann,^{1,6} and Norman Y. Yao^{1,2}

¹*Department of Physics, Harvard University, 17 Oxford St., MA 02138, USA*

²*Harvard Quantum Initiative, 60 Oxford St., MA 02138, USA*

³*Cavendish Laboratory, University of Cambridge, Cambridge CB3 0HE, United Kingdom*

⁴*Department of Physics and Arnold Sommerfeld Center for Theoretical Physics (ASC),*

Ludwig-Maximilians-Universität München, Theresienstrasse 37, München D-80333, Germany

⁵*Munich Center for Quantum Science and Technology (MCQST), Schellingstrasse 4, D-80799 München, Germany*

⁶*Department of Physics, Boston University, 590 Commonwealth Avenue, Boston, Massachusetts 02215, USA*

(Dated: December 11, 2025)

Quantum spin liquids are elusive long-range entangled states. Motivated by experiments in Rydberg quantum simulators, recent excitement has centered on the possibility of dynamically preparing a state with quantum spin liquid correlation even when the ground state phase diagram does not exhibit such a topological phase. Understanding the microscopic nature of such quantum spin “lake” states and their relationship to equilibrium spin liquid order remains an essential question. Here, we extend the use of approximately symmetric neural quantum states for real-time evolution and directly simulate the dynamical preparation in systems of up to $N = 384$ atoms. We analyze a variety of spin liquid diagnostics as a function of the preparation protocol and optimize the extent of the quantum spin lake thus obtained. In the optimal case, the prepared state shows spin-liquid properties extending over half the system size, with a topological entanglement entropy plateauing close to $\gamma = \ln 2$. We extract two physical length scales λ and ξ which constrain the extent of the quantum spin lake ℓ from above and below.

Quantum spin liquids (QSLs) are exotic phases of matter exhibiting macroscopic entanglement, fractionalized excitations, and emergent gauge symmetry [1–3]. Realizing and characterizing such spin liquid ground states have remained a long-standing challenge, motivating sustained efforts across both the quantum materials and quantum simulation communities [4–8]. On the materials front, while numerous spin-liquid candidates have been identified, positive signatures of spin-liquid behavior remain relatively scarce [9–13].

Quantum simulators offer alternative routes to engineering spin liquids. On digital platforms, spin liquid states can be prepared via projective measurements and feedback [14–16]. For analog simulators, a more conventional strategy is to prepare the spin liquid coherently via the quantum adiabatic theorem [17–24]. This approach relies upon slowly tuning the Hamiltonian such that the system remains in its instantaneous ground state throughout the time evolution, ultimately ending in the spin liquid phase. Recent experimental observations on a Rydberg quantum simulator suggest that this strategy may be even more effective than expected [7]: it may be possible to dynamically “ramp” into a spin-liquid state even when the underlying Hamiltonian *does not* host a QSL ground state [6].

This surprising possibility has ignited intense discussion about the nature of such dynamically generated states [25–29]. On the one hand, physical arguments [26] have been proposed to explain why spin-liquid correlations may naturally emerge over finite length scales up to a cutoff ℓ , defining a so-called “quantum spin lake.” On the other hand, equilibrium quantum Monte Carlo has

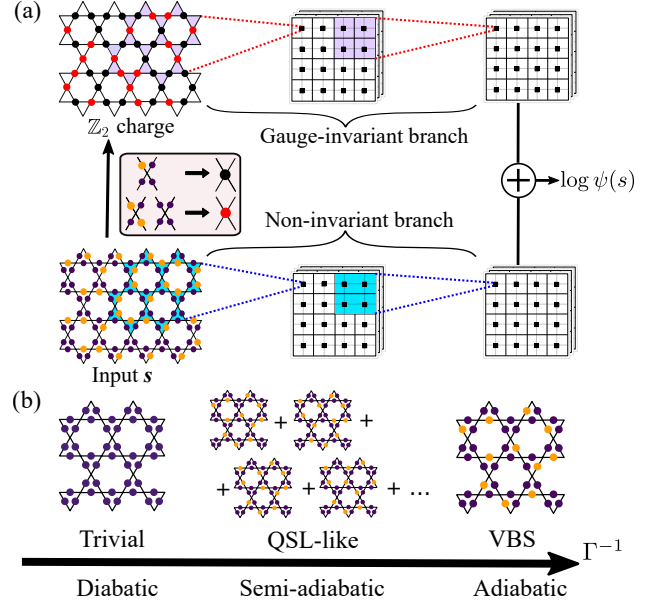


FIG. 1. (a) The approximately gauge-symmetric neural network architecture, comprising an exactly symmetric path (upper) and an unconstrained path (lower). The symmetric path takes as input the parity of the number of Rydberg states on atoms adjacent to each vertex of the kagome lattice. (b) Dynamical preparation of a QSL by ramping the Hamiltonian to excite more atoms from the ground state (purple) to the Rydberg state (orange) subjected to Rydberg blockade.

questioned the state’s quantum coherence and showed strong electric-channel area-law scaling [29], whereas time-dependent variational Monte Carlo reported a non-

quantized topological entanglement entropy [27].

In this Letter, we reconcile these differing perspectives via large-scale numerical simulations of dynamical spin liquid preparation using neural quantum states (NQS). Our main results are three-fold: First, by combining approximately symmetric neural network architectures [30] with a mean-field ansatz and enhanced regularization [Fig. 1(a)], we perform the highest-fidelity simulations of the experimental ramp protocol to date; in addition to investigating larger system sizes (up to $N = 384$) and longer time-scales than the experiment, we also explore generalizations of the ramp protocol. Second, we systematically analyze various spin liquid diagnostics as a function of the Hamiltonian ramp rate: when the ramp is too slow, one reverts to the adiabatic strategy and ends up in the actual (non-spin-liquid) ground state; when the ramp is too fast, one remains in the trivial initial state. For intermediate ramp rates, we demonstrate the emergence of quantum spin lakes [Fig. 1(b)], whose topological entanglement entropy matches that expected for a \mathbb{Z}_2 QSL; crucially, this is *despite* the fact that one type of Wilson loop exhibits an area-law scaling rather than the perimeter law characteristic of an equilibrium spin liquid. We reconcile these observations within an anyon gas framework, which enables us to both: (i) directly quantify the maximum spatial extent of any quantum spin lake that can be prepared, and (ii) provides guidance on how to optimize such a spin-lake preparation protocol.

Rydberg Hamiltonian and neural quantum states.—Let us begin by defining the setting. Consider a Rydberg quantum simulator with N neutral atoms arranged on a ruby lattice (i.e. links of a kagome lattice) [Fig. 1]. Each atom behaves as an effective two-level system defined by the electronic ground-state and a highly-excited Rydberg state: $\{|g\rangle, |r\rangle\}$. In the presence of an optical drive addressing the ground-Rydberg transition, the many-body Hamiltonian governing the system is given by:

$$H = -\frac{\Omega}{2} \sum_i (b_i + b_i^\dagger) + \sum_{ij} V_{ij} n_i n_j - \delta \sum_i n_i \quad (1)$$

where b_i^\dagger creates a Rydberg excitation at site i , $n_i = b_i^\dagger b_i$, Ω is the Rabi frequency of the optical drive while δ is the detuning, and $V_{ij} = \Omega(R_b/R_{ij})^6$ where R_b is the blockade radius.

The Hamiltonian (1) can be best understood working from the idealized ‘PXP’ limit, which corresponds to an infinite repulsion within the blockade radius $R_b = 2a$ (a denotes the spacing between atoms within a triangle) and no further interaction tail [6]. The PXP system exhibits a \mathbb{Z}_2 spin-liquid ground state for $1.4 \lesssim \delta/\Omega \lesssim 2.0$. Intuitively, the nature of the spin-liquid can be understood by considering each Rydberg excitation as a dimer on the kagome lattice. Around each kagome vertex, exactly one of the four surrounding atoms is in the Rydberg state [Fig. 1(b)], which constitutes a local Gauss’

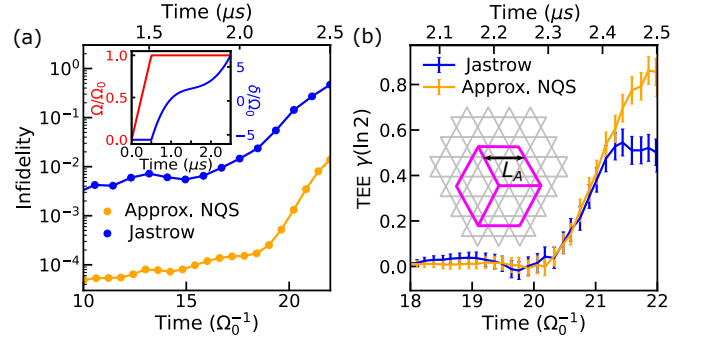


FIG. 2. (a) Infidelity of the approximately-symmetric NQS (orange dots) and Jastrow ansatz in Ref. [27] (blue squares) on $N = 24$ system under the ramping profile of Ref. [7] (inset) as compared with exact diagonalization. (b) Comparison of the TEE (γ) from approximately-symmetric NQS (orange) and Jastrow ansatz (blue) on an experimentally studied $N = 219$ system with open boundary conditions. The inset shows the geometry of the lattice and the partitions (red borders) used to compute the TEE at scale L_A .

law. The quantum spin liquid arises through the coherent superposition of all states satisfying this Gauss’ law [31, 32], which is believed to be adiabatically connected to the toric-code-like model referred to as the stabilizer limit below. Unfortunately, the PXP spin-liquid ground state appears to be unstable to the reintroduction of the long-range tails of the van der Waals interaction (i.e. $V_{ij} \sim 1/R_{ij}^6$). This was shown by tensor network methods studying the zero-temperature phase diagram of Eqn. (1) [6], which we corroborate using large-scale NQS simulations in the End Matter.

The experimental dynamical protocol starts from the product state $|g\rangle^{\otimes N}$ and ramps both $\Omega(t)$ and $\delta(t)$ [inset, Fig. 2(a)]. In order to study the states thus prepared, we utilize neural quantum states (NQS). Within the NQS framework, a quantum state is represented as $|\psi\rangle = \sum_s \psi(s) |s\rangle$, where a neural network maps a basis configuration s to a complex amplitude $\psi(s)$ [33]. The past several years have witnessed rapid progress in NQS methods, with state-of-the-art results obtained for both quantum ground-state [33–37], steady states of open systems [38–41], and dynamics problems [42–44]. In the context of Rydberg quantum simulation, a key advantage of NQS-based methods compared to other numerical approaches is the ability to directly simulate experimentally-relevant geometries and system sizes [27]. Crucially, in order to improve both the accuracy and robustness of our NQS simulations, we utilize approximately-symmetric neural networks [30] which are able to capture the emergent gauge symmetries of the purported quantum spin liquid [Fig. 1(a)].

The gauge symmetries are easiest to understand and visualize in the stabilizer limit of the PXP spin-liquid. In this limit, one restricts the Hilbert space of three

atoms on a triangle to the single-excitation subspace $\{|ggg\rangle, |rgg\rangle, |grg\rangle, |ggr\rangle\}$, which naturally occurs in the regime of strong intra-triangle blockade. The stabilizer Hamiltonian is then given by:

$$\begin{aligned}
 H_s &= \sum_{v \in \mathbb{X}} \underbrace{\text{Diagram of } A_v}_{A_v} - \sum_{p \in \mathbb{Y}} \underbrace{\text{Diagram of } B_p}_{B_p} \\
 \mathcal{Z}_l &= \text{Diagram of } \mathcal{Z}_l = |\text{purple dot}\rangle\langle\text{orange dot}| - |\text{orange dot}\rangle\langle\text{purple dot}| \\
 \mathcal{X}_l &= \text{Diagram of } \mathcal{X}_l = |\text{purple dot}\rangle\langle\text{orange dot}| + |\text{orange dot}\rangle\langle\text{purple dot}| + h.c.
 \end{aligned} \tag{2}$$

Here, we work with a convenient visual representation of the operators that enter H_s [32]. In particular, the dashed red line corresponds to a \mathcal{Z} operator that assigns +1 to the ground state (purple dot) and -1 to the Rydberg-state (orange dot), while the wavy blue line corresponds to an \mathcal{X} operator that creates or shuffles a “Rydberg dimer” around the triangle [32]. Using this representation, the two terms in the stabilizer Hamiltonian correspond to: (i) the sum of A_v -product of \mathcal{Z} around one vertex and (ii) the sum of B_p -product of \mathcal{X} over one hexagonal plaquette. Physically, the former enforces the local Gauss’ law, while the latter induces resonances among Gauss’-law-obeying configurations. Since all A_v and B_p commute, H_s exhibits an exponentially large group of local symmetries, $G = \mathbb{Z}_2 \times \mathbb{Z}_2 \times \dots \times \mathbb{Z}_2$, making it naturally suited for a gauge-invariant neural network architecture [45, 46].

Beyond the stabilizer limit, one still expects an exponentially large group of emergent symmetries in the spin liquid, although their explicit microscopic form is no longer known. To handle this, we utilize an architecture with two branches [30]: (i) a gauge-invariant branch that explicitly respects the symmetries generated by B_p s in the stabilizer limit described above and (ii) a generic, non-invariant branch capable of representing the emergent symmetries away from the stabilizer limit. For the gauge-invariant branch [top, Fig. 1(a)], one begins by computing A_v (from a configuration s) centered on each vertex [Eqn. 2]. These \mathbb{Z}_2 charges (Fig. 1a) then become the input for our gauge-invariant branch and are processed through multiple layers of a convolutional neural network [47]. By contrast, our non-invariant branch [bottom, Fig. 1(a)], operates directly on the input configuration s and is thus unconstrained. Finally, the outputs from both branches are combined element-wise to produce the logarithmic amplitude of each basis state $\log \psi_s$ [Fig. 1(a)]. To further enhance the robustness of our approximately-symmetric neural network against rare, high-energy configurations that destabilise the simulation, we also incorporate a mean-field ansatz into the architecture (see End Matter and [47]).

Preparing a dynamical quantum spin liquid—In order to simulate the dynamical preparation protocol, we utilize our approximately-symmetric NQS within the time-dependent variational principle (TDVP) [47, 48]. As a

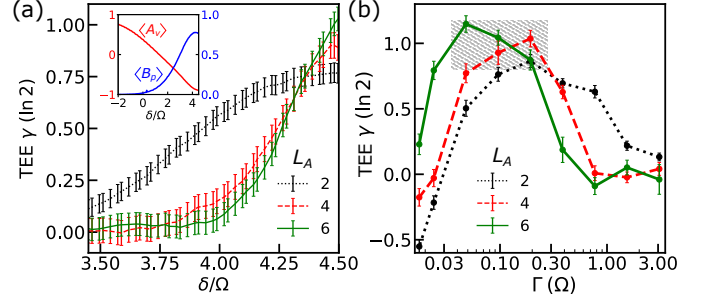


FIG. 3. Optimizing preparation protocol for spin lake. (a) Topological entanglement entropy with ramping rate $\Gamma \approx 0.096 \Omega$ varying the final δ . The inset shows the evolution of stabilizers A_v and B_p with final δ over a wider range. (b) Topological entanglement entropy over different subsystems (see Fig. S3(b) in [47]) fixing the final $\delta/\Omega = 4.5$ and varying the ramp rate Γ . The hatched region indicates a proxy for finite-size spin-liquid-like behavior over the range $\Gamma \sim 0.03$ to ~ 0.2 with a TEE close to $\ln 2$. The subsystem size L_A is depicted in the inset of Fig. 2(b).

benchmark, we begin by directly simulating the ramping profile implemented in the Rydberg experiment [inset, Fig. 2(a)] [7]; we note that a recent work has also explored these dynamics via TDVP using a decorated Jastrow ansatz [27]. Working at small system sizes ($N = 24$), Figure 2(a) depicts the state infidelity as a function of the ramp time for both ansatzes compared to exact diagonalization. The approximately-symmetric NQS exhibits an infidelity nearly two orders of magnitude lower across the entirety of the ramping protocol; this is especially important near the end of the dynamical spin liquid preparation where the state obtained by the Jastrow ansatz exhibits a $\sim 50\%$ infidelity, while the state obtained via NQS exhibits a $\sim 1\%$ infidelity [49].

Building on these fidelities, we now directly simulate the preparation dynamics on significantly larger system sizes ($N = 219$) using the precise experimental geometry (inset, Fig. 2b). To quantify the topological nature of the prepared state, we track the topological entanglement entropy of the state. Even though a protecting energy gap is not present in this context, a nearly quantized TEE still distinguishes good spin liquid-like properties from poor ones on mesoscopic length scales. For this geometry, Jastrow ansatz simulations observe a gradual rise in the TEE at scale $L_A = 4$ (about half the system size) as a function of the ramping time [blue curve, Fig. 2(b)]; however, the TEE does not saturate anywhere near the value expected ($\gamma = \ln 2$) for a \mathbb{Z}_2 spin liquid, leading previous authors to the conclusion that the state does not exhibit a true \mathbb{Z}_2 topological order [27]. For early times during the ramp, our NQS simulations closely match the Jastrow numerics, but near the end—when the state begins to develop a nonzero TEE—the two methods diverge. In particular, we observe a final state which exhibits a TEE close to that of a \mathbb{Z}_2 spin liquid [orange curve, Fig. 2(b)].

Optimizing the preparation protocol—We take the observation of TEE $\gamma \approx \ln 2$ as positive evidence that the state prepared by the dynamical protocol is indeed a ‘spin lake’ state [26] for $\ell \gtrsim L_A = 4$. We now optimize the preparation protocol in order to maximize the spin-lake size ℓ . To simplify the investigation, we use linear ramps and a larger Rydberg-atom lattice with periodic boundary conditions and $N = 384$ atoms. The linear ramp is engineered so that the Rabi frequency Ω and blockade radius $R_b = 2.4 a$ are fixed while the detuning is swept from the trivial phase $\delta/\Omega = -2$ at a constant rate Γ . In the inset of Fig. 3(a), we roughly tune the protocol by fixing the rate $\Gamma \approx 0.1 \Omega$ and measuring the $\langle A_v \rangle$ and $\langle B_p \rangle$ as a function of the final detuning δ of the ramp. We find that $\langle A_v \rangle$ approaches -1 and $\langle B_p \rangle$ approaches $+1$, as expected of the stabilizer Hamiltonian ground state spin liquid, around $\delta/\Omega \approx 4.5$, squarely in the ground state VBS phase. We confirm the topological nature of the prepared state by computing the scaling of TEE with the subsystem size L_A in Fig. 3(a). Near the optimal $\delta/\Omega \approx 4.5$, we observe a consistent improvement of TEE with larger subsystems up to $L_A = 6$ (the largest size available without touching the boundaries). This suggests that the spin lake prepared by sweeping into the VBS phase is much larger than the lattice scale and comparable with the lattice size (linear scale of 16 kagome links). Remarkably, as demonstrated in Fig. 3(b), the extent of the spin lake is also governed by the ramp rate. Fixing the final detuning at $\delta/\Omega = 4.5$, the TEE first increases as the ramp rate is slowed, reaching a value near $\ln 2$, before subsequently decreasing back to zero for adiabatic ramps. Focusing on the largest subsystem $L_A = 6$, one can identify an optimal ramping rate around which the TEE is close to $\ln 2$ [the hatched region in Fig. 3(b)].

Characterizing the prepared spin lake—The TEE provides a numerically concise, basis-independent, diagnostic of spin liquid correlations, but, ultimately, spin liquids are physically understood in terms of their anyonic excitations. These are encoded in the Wilson loop $W_A^{\mathcal{Z}/\mathcal{X}}$ and open string operators $S_L^{\mathcal{X}/\mathcal{Z}}$ which measure the correlations of the underlying e and m -type anyons of the \mathbb{Z}_2 liquid (in the stabilizer limit, e is a violation of $A_v = -1$ and m is a violation of $B_p = +1$). We use the string and loop operators inherited from the stabilizer limit, although this requires some care as the ‘true’ operators governing physical e and m anyons would, even in a true equilibrium phase, be fattened [50].

Let us begin with the \mathcal{Z} Wilson loop. Naively, in a \mathbb{Z}_2 deconfined phase, this should exhibit a perimeter law with a length scale governed by the pair fluctuations of e anyons. However, $W^{\mathcal{Z}}$ measured on the prepared state shows deviations from the perimeter law [47], similar to the equilibrium Monte-Carlo results [29]. We hypothesize that these deviations reflect an area-law scaling due to the presence of a free dilute gas of e -anyons. The num-

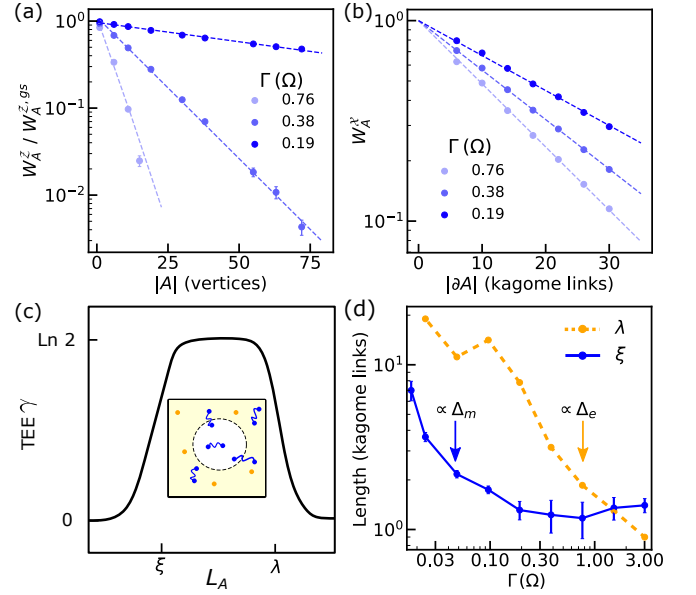


FIG. 4. (a) The area-law scaling of $W_A^{\mathcal{Z}}/W_A^{\mathcal{Z},gs}$ at different ramp rates. (b) The perimeter-law scaling of $W_A^{\mathcal{X}}$. (c) Pictorial depiction of TEE with respect to length scale L_A of the subsystem A . TEE approaches $\ln 2$ for $\lambda > L_A > \xi$. The inset shows the free e -gas with average distance λ and tightly bound m -pairs with pair length ξ . (d) The upper limit λ for the dynamical spin liquid size defined by the average distance between unbound leftover e -anyons, the lower limit ξ defined by the m -anyon pair length. For each length scale, the adiabatic limit is set by the energy scale of the respective excitation species.

ber of e ’s in a region A fluctuates statistically, with the probability of finding k anyons exhibiting a Poisson distribution, $P(k) = \alpha^k e^{-\alpha}/k!$ where $\alpha = |A|/2\lambda^2$ is the average number of e anyons in the region A . In this model, the parity of e anyons enclosed in A is

$$\sum_k P(k)(-1)^k = (-1)^{|A|} e^{-|A|/\lambda^2}, \quad (3)$$

producing an area-law decay. This area-law is superimposed on a perimeter law coming from the virtual e -pair fluctuations in the true, adiabatic, ground state of H . As shown in Fig. 4(a), after dividing out the corresponding loops evaluated in the ground state, $W_A^{\mathcal{Z}}/W_A^{\mathcal{Z},gs}$ exhibits a pure area-law scaling. Extrapolating Eqn. 3 to the elementary loop surrounding one vertex, we can relate the scaling coefficient with the defect concentration by $1/\lambda^2 = 2(n_e - n_e^{gs})$ where $n_e = (1 + \langle A_v \rangle)/2$. We numerically verify this simple, but non-trivial, relationship between three observable quantities in [47].

In contrast, the \mathcal{X} Wilson loop $W_A^{\mathcal{X}}$ scaling exhibits the perimeter law expected of a deconfined spin liquid [Fig. 4(b)]. Since \mathcal{X} -loop operators anti-commute with open \mathcal{Z} string operators $S_L^{\mathcal{Z}}$, the perimeter law of $W_A^{\mathcal{X}}$ suggests a finite length scale for the decay of the open string $S_L^{\mathcal{Z}} \propto e^{-L/\xi}$ which probes m -pair correlations [47].

We now argue that the two length scales, λ and ξ , govern the extent of the spin lake. At long length scales ℓ , the state has to be an e -condensate because it is connected to the initial trivial state by a finite-time evolution. During the preparation, this e -condensate (equivalent to $|+\rangle^{\otimes N}$ in the toric code) is perturbatively acted on by \mathcal{Z} -loops and \mathcal{Z} -string with characteristic lengths λ and ξ , respectively. For a subsystem A such that $L_A > \lambda, \xi$, the \mathcal{Z} -type perturbations become irrelevant, producing a trivial-state with TEE $\gamma \approx 0$. For $\lambda > L_A > \xi$, the \mathcal{Z} loops become relevant and condense while the \mathcal{Z} -strings are suppressed, resulting in the \mathbb{Z}_2 -spin liquid correlations with $\gamma \approx \ln 2$. Lastly, at the short scale $L_A < \xi$, \mathcal{Z} -strings condense generating VBS-like characteristics with vanishing TEE. In summary, TEE varies non-monotonically with the length scale L_A , approaching the quantized value $\ln 2$ in the window between ξ and λ as shown pictorially in Fig. 4(c).

The upper and lower bounds on the spatial extent ℓ of the spin lake can be understood within the anyon picture. Therein, $\lambda = 1/\sqrt{\eta} \sim 1/\sqrt{n_e}$ gives the average distance between free e anyons and ξ characterizes the length of m pairs since a \mathcal{Z} -string acting on the e -condensate produces an m pair. First, L_A must be larger than ξ so that the contribution of m anyon pairs arises only from crossings at the boundary. This is not possible for very slow ramps, when a VBS is formed. Second, L_A must be smaller than λ to ensure that the number of enclosed e anyons is negligible, preserving the Gauss' law character of the state. This is not possible for very fast ramps, when the final state is trivial. Thus, only for intermediate ramps can one obtain a separation of scales between λ and ξ and observe topological correlations for spatial regions satisfying $\lambda \gtrsim L_A \gtrsim \xi$ [inset of Fig. 4(c)]. That such a regime exists relies on the difference between the energy gaps Δ_e and Δ_m controlling the non-adiabatic production of e and m -anyons during the ramp. Although these gaps are only loosely defined—since the Rydberg Hamiltonian governing the dynamics [Eq. (1)] differs from the stabilizer-limit Hamiltonian [Eq. (2)]—we estimate them as the energy cost of open string operators acting on the optimally prepared state, evaluated with respect to the final Hamiltonian. Somewhat surprisingly, the separation of these energy scales roughly corresponds to the crossover scales in λ and ξ as a function of ramp rate Γ [Fig. 4(d)] [51] and the largest length scale separation is achieved for $\Delta_e \gtrsim \Gamma \gtrsim \Delta_m$. Compared with the TEE measure in Fig. 3(b), Fig. 4(d) qualitatively reproduces the optimal ramp rate at different length scales.

Outlook.—Our large-scale NQS-based study clarifies how to optimally generate substantial quantum spin-lake states and provides guidance on next-generation Rydberg simulators with larger lattices and longer coherence times [52]. The NQS architecture can be generalized to other types of topological orders such as the \mathbb{Z}_3 [53] and especially $U(1)$ [26] quantum spin liquid where there exists no

stable equilibrium analog in 2D. Moreover, non-Abelian topological orders [15, 54] can also be captured within our framework. It is interesting to study how the non-abelian braiding of anyons might affect the dynamical preparation of such phases. Finally, our simulation can extend to the thermalization dynamics after preparation, revealing the stability of dynamical spin liquids.

Acknowledgements—We gratefully acknowledge the insights of and discussions with Marcus Bintz, Johannes Feldmeier, Brenden Roberts, Rahul Sahay, Giulia Semeghini, and Peter Zoller. This work was supported by the U.S. Department of Energy via the Office of Science, National Quantum Information Science Research Centers, Quantum Systems Accelerator. J.K. acknowledges support from NSF through the Center for Ultracold Atoms and via EPSRC Grant No. EP/V062654/1. D.K. acknowledges support from a Generation-Q AWS fellowship. L.P. acknowledges support from the Deutsche Forschungsgemeinschaft (DFG, German Research Foundation) under Germany's Excellence Strategy – EXC-2111 – project number 390814868. The project/research is part of the Munich Quantum Valley, which is supported by the Bavarian state government with funds from the Hightech Agenda Bayern Plus. L.P. thanks Harvard University for its hospitality. C.R.L. acknowledges the Gutzwiller Fellowship at Max Planck Institute for the Physics of Complex Systems and the partial support of SFB 1143 and ct.qmat.

* These authors contributed equally to this work.

- [1] P. W. Anderson, Resonating valence bonds: A new kind of insulator?, *Materials Research Bulletin* **8**, 153 (1973).
- [2] A. Kitaev and J. Preskill, Topological entanglement entropy, *Physical Review Letters* **96**, 110404 (2006).
- [3] L. Savary and L. Balents, Quantum spin liquids: a review, *Reports on Progress in Physics* **80**, 016502 (2016).
- [4] Y. Shimizu, K. Miyagawa, K. Kanoda, M. Maesato, and G. Saito, Spin liquid state in an organic mott insulator with a triangular lattice, *Physical Review Letters* **91**, 107001 (2003).
- [5] J. Wen, S.-L. Yu, S. Li, W. Yu, and J.-X. Li, Experimental identification of quantum spin liquids, *npj Quantum Materials* **4**, 12 (2019).
- [6] R. Verresen, M. D. Lukin, and A. Vishwanath, Prediction of toric code topological order from rydberg blockade, *Physical Review X* **11**, 031005 (2021).
- [7] G. Semeghini, H. Levine, A. Keesling, S. Ebadi, T. T. Wang, D. Bluvstein, R. Verresen, H. Pichler, M. Kalinowski, R. Samajdar, *et al.*, Probing topological spin liquids on a programmable quantum simulator, *Science* **374**, 1242 (2021).
- [8] J. Knolle and R. Moessner, A field guide to spin liquids, *Annual Review of Condensed Matter Physics* **10**, 451–472 (2019).
- [9] P. Czajka, T. Gao, M. Hirschberger, P. Lampen-Kelley, A. Banerjee, J. Yan, D. G. Mandrus, S. E. Nagler, and

- N. P. Ong, Oscillations of the thermal conductivity in the spin-liquid state of α - RuCl_3 , *Nature Physics* **17**, 915 (2021).
- [10] Z. Zeng, C. Zhou, H. Zhou, L. Han, R. Chi, K. Li, M. Kofu, K. Nakajima, Y. Wei, W. Zhang, D. G. Mazzone, Z. Y. Meng, and S. Li, Spectral evidence for dirac spinons in a kagome lattice antiferromagnet, *Nature Physics* **20**, 1097 (2024).
- [11] G. Zheng, Y. Zhu, K.-W. Chen, B. Kang, D. Zhang, K. Jenkins, A. Chan, Z. Zeng, A. Xu, O. A. Valenzuela, J. Blawat, J. Singleton, P. A. Lee, S. Li, and L. Li, Unconventional magnetic oscillations in a kagome mott insulator, *Proceedings of the National Academy of Sciences* **122**, e2421390122 (2025).
- [12] J. A. N. Bruin, R. R. Claus, Y. Matsumoto, N. Kurita, H. Tanaka, and H. Takagi, Robustness of the thermal hall effect close to half-quantization in a field-induced spin liquid state, *Nature Physics* **18**, 401 (2022).
- [13] P. Czaika, T. Gao, M. Hirschberger, P. Lampen-Kelley, A. Banerjee, N. Quirk, D. G. Mandrus, S. E. Nagler, and N. P. Ong, Planar thermal hall effect of topological bosons in the kitaev magnet α - RuCl_3 , *Nature Materials* **22**, 36 (2023).
- [14] K. Satzinger, Y.-J. Liu, A. Smith, C. Knapp, M. Newman, C. Jones, Z. Chen, C. Quintana, X. Mi, A. Dunsworth, *et al.*, Realizing topologically ordered states on a quantum processor, *Science* **374**, 1237 (2021).
- [15] M. Iqbal, N. Tantivasadakarn, R. Verresen, S. L. Campbell, J. M. Dreiling, C. Figgatt, J. P. Gaebler, J. Johansen, M. Mills, S. A. Moses, *et al.*, Non-abelian topological order and anyons on a trapped-ion processor, *Nature* **626**, 505 (2024).
- [16] M. Iqbal, A. Lyons, C. F. B. Lo, N. Tantivasadakarn, J. Dreiling, C. Foltz, T. M. Gatterman, D. Gresh, N. Hewitt, C. A. Holliman, *et al.*, Qutrit toric code and parafermions in trapped ions, *Nature Communications* **16**, 6301 (2025).
- [17] E. Farhi, J. Goldstone, S. Gutmann, and M. Sipser, Quantum computation by adiabatic evolution, *arXiv preprint quant-ph/0001106* (2000).
- [18] A. Hama and D. A. Lidar, Adiabatic preparation of topological order, *Physical review letters* **100**, 030502 (2008).
- [19] R. Islam, C. Senko, W. C. Campbell, S. Korenblit, J. Smith, A. Lee, E. Edwards, C.-C. Wang, J. Freericks, and C. Monroe, Emergence and frustration of magnetism with variable-range interactions in a quantum simulator, *science* **340**, 583 (2013).
- [20] Preparing atomic topological quantum matter by adiabatic nonunitary dynamics, .
- [21] S. Ebadi, T. T. Wang, H. Levine, A. Keesling, G. Semeghini, A. Omran, D. Bluvstein, R. Samajdar, H. Pichler, W. W. Ho, *et al.*, Quantum phases of matter on a 256-atom programmable quantum simulator, *Nature* **595**, 227 (2021).
- [22] M. Mambri and D. Poilblanc, Quantum state preparation of topological chiral spin liquids via floquet engineering, *SciPost Physics* **17**, 011 (2024).
- [23] T. Cookmeyer and S. Das Sarma, Engineering the kitaev spin liquid in a quantum dot system, *Physical Review Letters* **132**, 186501 (2024).
- [24] M. Bintz, V. S. Liu, J. Hauschild, A. Khalifa, S. Chatterjee, M. P. Zaletel, and N. Y. Yao, Dirac spin liquid in quantum dipole arrays, *arXiv preprint arXiv:2406.00098* (2024).
- [25] G. Giudici, M. D. Lukin, and H. Pichler, Dynamical preparation of quantum spin liquids in rydberg atom arrays, *Physical Review Letters* **129**, 090401 (2022).
- [26] R. Sahay, A. Vishwanath, and R. Verresen, Quantum spin puddles and lakes: Nisq-era spin liquids from non-equilibrium dynamics (2023), *arXiv:2211.01381 [cond-mat.str-el]*.
- [27] L. Mauron, Z. Denis, J. Nys, and G. Carleo, Predicting topological entanglement entropy in a rydberg analogue simulator, *Nature physics* , 1 (2025).
- [28] P. Patil, Quantum monte carlo simulations in the restricted hilbert space of rydberg atom arrays (2025), *arXiv:2309.00482 [cond-mat.str-el]*.
- [29] Z. Wang and L. Pollet, Renormalized classical spin liquid on the ruby lattice, *Physical Review Letters* **134**, 086601 (2025).
- [30] D. S. Kufel, J. Kemp, D. Vu, S. M. Linsel, C. R. Laumann, and N. Y. Yao, Approximately symmetric neural networks for quantum spin liquids, *Physical Review Letters* **135**, 056702 (2025).
- [31] G. Misguich, D. Serban, and V. Pasquier, Quantum dimer model on the kagome lattice: Solvable dimer-liquid and ising gauge theory, *Physical Reivew Letters* **89**, 137202 (2002).
- [32] R. Verresen and A. Vishwanath, Unifying kitaev magnets, kagomé dimer models, and ruby rydberg spin liquids, *Physical Review X* **12**, 041029 (2022).
- [33] G. Carleo and M. Troyer, Solving the quantum many-body problem with artificial neural networks, *Science* **355**, 602 (2017).
- [34] K. Choo, G. Carleo, N. Regnault, and T. Neupert, Symmetries and many-body excitations with neural-network quantum states, *Physical Review Letters* **121**, 167204 (2018).
- [35] D. Luo and B. K. Clark, Backflow transformations via neural networks for quantum many-body wave functions, *Physical Review Letters* **122**, 226401 (2019).
- [36] K. Choo, T. Neupert, and G. Carleo, Two-dimensional frustrated J_1 – J_2 model studied with neural network quantum states, *Physical Review B* **100**, 125124 (2019).
- [37] C. Roth, A. Szabó, and A. H. MacDonald, High-accuracy variational monte carlo for frustrated magnets with deep neural networks, *Physical Review B* **108**, 054410 (2023).
- [38] G. Torlai and R. G. Melko, Latent space purification via neural density operators, *Physical Review Letters* **120**, 240503 (2018).
- [39] J. Carrasquilla, G. Torlai, R. G. Melko, and L. Aolita, Reconstructing quantum states with generative models, *Nature Machine Intelligence* **1**, 155 (2019).
- [40] Y. Nomura, N. Yoshioka, and F. Nori, Purifying deep boltzmann machines for thermal quantum states, *Physical Review Letters* **127**, 060601 (2021).
- [41] D. Wagner, A. Klümper, and J. Sirker, Thermodynamics based on neural networks, *Physical Review B* **109**, 155128 (2024).
- [42] M. Schmitt and M. Heyl, Quantum many-body dynamics in two dimensions with artificial neural networks, *Physical Review Letters* **125**, 100503 (2020).
- [43] T. Mendes-Santos, M. Schmitt, and M. Heyl, Highly resolved spectral functions of two-dimensional systems with neural quantum states, *Physical Review Letters* **131**, 046501 (2023).
- [44] M. Schmitt, M. M. Rams, J. Dziarmaga, M. Heyl, and

END MATTER

- W. H. Zurek, Quantum phase transition dynamics in the two-dimensional transverse-field ising model, *Science Advances* **8**, eabl6850 (2022).
- [45] D. Luo, G. Carleo, B. K. Clark, and J. Stokes, Gauge equivariant neural networks for quantum lattice gauge theories, *Physical Review Letters* **127**, 276402 (2021).
 - [46] D. Luo, Z. Chen, K. Hu, Z. Zhao, V. M. Hur, and B. K. Clark, Gauge-invariant and anyonic-symmetric autoregressive neural network for quantum lattice models, *Physical Review Research* **5**, 013216 (2023).
 - [47] See the Supplemental Material for detailed information on numerical methods, benchmarks and additional data.,.
 - [48] P. Kramer and M. Saraceno, *Geometry of the Time-Dependent Variational Principle in Quantum Mechanics*, 1st ed., Lecture Notes in Physics, 140 (Springer Berlin Heidelberg, Berlin, Heidelberg, 1981).
 - [49] We note that directly optimizing with respect to the exact state yields an additional order-of-magnitude improvement in the infidelity for the approximately-symmetric NQS. This improvement is not seen for the Jastrow ansatz [47].
 - [50] M. B. Hastings and X.-G. Wen, Quasiadiabatic continuation of quantum states: The stability of topological ground-state degeneracy and emergent gauge invariance, *Physical Review B* **72**, 045141 (2005).
 - [51] Quantitatively, we find $\Delta_e \approx 3.09 \Omega$ and $\Delta_m \approx 0.19 \Omega$.
 - [52] H. J. Manetsch, G. Nomura, E. Bataille, X. Lv, K. H. Leung, and M. Endres, A tweezer array with 6100 highly coherent atomic qubits, *Nature*, **1** (2025).
 - [53] G. Giudice, F. M. Surace, H. Pichler, and G. Giudici, Trimer states with z_3 topological order in rydberg atom arrays, *Physical Review B* **106**, 195155 (2022).
 - [54] S. Xu, Z.-Z. Sun, K. Wang, H. Li, Z. Zhu, H. Dong, J. Deng, X. Zhang, J. Chen, Y. Wu, *et al.*, Non-abelian braiding of fibonacci anyons with a superconducting processor, *Nature Physics* **20**, 1469 (2024).
 - [55] P. Ramachandran, B. Zoph, and Q. V. Le, Searching for activation functions, *arXiv preprint arXiv:1710.05941* (2017).
 - [56] A. Sinibaldi, C. Giuliani, G. Carleo, and F. Vicentini, Unbiasing time-dependent Variational Monte Carlo by projected quantum evolution, *Quantum* **7**, 1131 (2023).
 - [57] L. Gravina, V. Savona, and F. Vicentini, Neural projected quantum dynamics: a systematic study (2024), *arXiv:2410.10720*.
 - [58] S. Sorella, Green function monte carlo with stochastic reconfiguration, *Physical Review Letters* **80**, 4558 (1998).
 - [59] A. N. Tikhonov, *Solutions of ill posed problems* (John Wiley & Sons, 1977).
 - [60] A. Vehtari, A. Gelman, D. Simpson, B. Carpenter, and P.-C. Bürkner, Rank-normalization, folding, and localization: An improved r for assessing convergence of mcmc (with discussion), *Bayesian Analysis* **16**, 667 (2021).
 - [61] M. B. Hastings, I. González, A. B. Kallin, and R. G. Melko, Measuring renyi entanglement entropy in quantum monte carlo simulations, *Physical Review Letters* **104**, 157201 (2010).
 - [62] E. Fradkin and S. H. Shenker, Phase diagrams of lattice gauge theories with higgs fields, *Physical Review D* **19**, 3682 (1979).

Ground state phase diagram— Using NQS we can map out the $T = 0$ phase diagram of the full $1/r^6$ Rydberg model. This phase diagram is under active debate and provides a baseline for our later dynamical study. Ref. [6], using iDMRG on infinite cylinders, argued that the full $1/r^6$ model does not host a QSL at any value of detuning at the largest truncation distances (unlike its PXP Hamiltonian limit). However, on finite cylinders the long-range interactions must be cut off along the compact direction, and the putative QSL depends on the cylinder width. We revisit this problem with NQS, which can accommodate arbitrary boundary conditions and avoid truncating long-range interactions.

Obtaining the ground state of the Rydberg-atom model involves two principal challenges: (i) The initial state is significantly far away from the true ground state, owing to the large number of blockade violations pushing up the energy; starting from such a high-energy state can cause the neural network to become unstable in the subsequent variational training. (ii) For $\delta \gg \Omega$, the solid-liquid energy splitting is small, and as a result, a randomly initialized ansatz is prone to becoming trapped in a liquid-like local minimum.

We resolve both issues by adding a mean-field component into the ansatz given by

$$\log \psi(s) = \theta^{MF}(s) + \theta^{NN}(s), \quad (4)$$

where $\theta^{NN}(s)$ is the output of the approximately gauge-symmetric neural network and $\theta^{MF}(s)$ is the mean-field ansatz $\theta^{MF}(s) = \sum_i s_i \left(A + \sum_{j: R_{ij} < R_b} B_{R_{ij}} s_j \right)$ with R_b denoting the blockade radius and $s_i = 1(-1)$ representing the ground state (Rydberg state) at site i . Taking into account equal distances, θ_{MF} is characterized by three parameters: A and two distinct values for $B_{R_{ij}}$.

To address issue (i), we first pretrain the mean-field component by fixing all parameters in θ^{NN} in Eqn. (4) and optimizing only those in θ^{MF} . Starting from a random initialization, the $B_{R_{ij}}$ parameters quickly acquire large negative values, effectively capturing the low probability of Gauss-law-violating configurations and yielding an energy close to the ground state. This pretrained state provides a stable foundation for subsequent refinement of the deep neural network.

To mitigate issue (ii), we guide the search toward specific symmetry-breaking patterns while still letting the lowest energy select the final state. Specifically, we relax translational symmetry in the mean-field ansatz by promoting the uniform parameter A to a site-dependent A_i , initialized as $A_i = \pm 1$ depending on the seeded ground/Rydberg state. We then compare the energies obtained from the VBS and SS initializations with those from a symmetric random start. We choose two initialization patterns: the valence bond solid (VBS) with

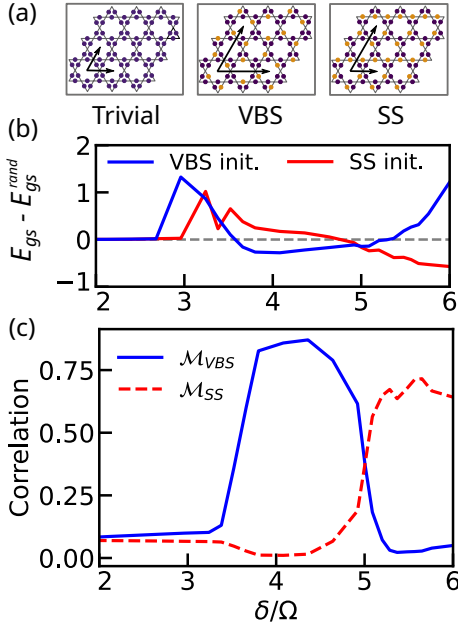


FIG. 5. Ground state phase diagram as a function δ/Ω . (a) Excitation pattern in the three phases: symmetric trivial, symmetry-breaking valence bond solid (VBS), and symmetry-breaking stripe solid (SS). The unit vectors in each phase are shown with arrows. The VBS state doubles the unit cell as the lattice in both unit vector directions, while the SS does so in one direction. (b) Ground state energy with VBS and SS initializations offset by E_{gs} computed with random initialization. (c) Correlations [as defined by Eqn. (5)] detecting the symmetry-breaking pattern of the VBS (blue solid) and SS (red dashed) phases.

Rydberg density $n_{Ryd} = 1/4$ and the stripe solid (SS) with $n_{Ryd} = 1/3$ [Fig. 5(a)]. The VBS spontaneously breaks the rotation and translation symmetries, doubling the unit vectors in both directions. In contrast, the SS phase breaks translation symmetry along only one axis, concentrating excitations along parallel lines. This structure arises because SS necessarily violates the inter-triangle Rydberg blockade; however, due to the $1/r^6$ interaction, $V(\text{triangle}) \approx 3\Omega$ is energetically less costly than $V(\text{triangle}) \approx 7\Omega$, making aligned Rydberg excitations more favorable. In Fig. 5(b), we observe that for sufficiently large δ , the solid-initialized state attains lower energy, indicating a transition to a solid ground state.

To distinguish between different symmetry-breaking patterns, we define the correlation:

$$\begin{aligned} \mathcal{M}_{VBS} &= \frac{1}{N_{\text{unit cell}}} \sum_{n_1, n_2} (-1)^{n_1+n_2} u_{n_1, n_2} \\ \mathcal{M}_{SS} &= \frac{1}{N_{\text{unit cell}}} \sum_{n_1, n_2} (-1)^{n_1} u_{n_1, n_2}, \end{aligned} \quad (5)$$

where n_1 and n_2 label unit cell positions as a multiple of the respective unit vectors \mathbf{a}_1 and \mathbf{a}_2 with \mathbf{a}_2 being the

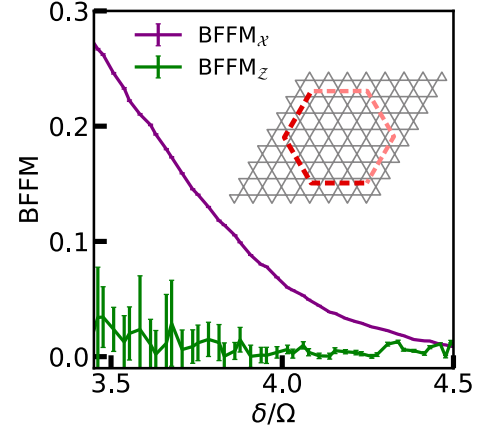


FIG. 6. BFFM order parameter with fixed $\Gamma \approx 0.096 \Omega$. Both the diagonal and off-diagonal BFFM order parameters approach zero as δ is swept into the VBS phase. The inset depicts the closed loop, and the open string corresponding to half that loop, used for computing the BFFM order parameters.

symmetric direction of the SS configuration. u_{n_1, n_2} is a binary variable which depends on the state s_{n_1, n_2} of the up-triangle in the unit cell at (n_1, n_2) . Specifically,

$$u_{n_1, n_2} = \begin{cases} s_{n_1, n_2} \circ s_{0,0} & \text{for even } n_1 \\ (s_{n_1, n_2} \circ s_{1,0}) (s_{1,0} \circ s_{0,0}) & \text{for odd } n_1 \end{cases}, \quad (6)$$

where $s \circ s' = 1$ if $s = s'$ and -1 otherwise. With this choice of u_{n_1, n_2} , the VBS and SS order parameters are maximized for the checkerboard and stripe patterns, respectively. As shown in Fig. 5(c), the order parameters \mathcal{M}_{VBS} and \mathcal{M}_{SS} become finite in their respective phases and diminish elsewhere, establishing two phase transitions: trivial-VBS at $\delta/\Omega \approx 3.4$ and VBS-SS at $\delta/\Omega \approx 5.2$.

String order parameter—In addition to the TEE over a finite subsystem, here we provide another finite-size metric for the topological order, namely the Brimont-Frölich-Fredenhagen-Marcu (BFFM) order parameter. The diagonal BFFM_Z characterizes the confinement of m excitations,

$$\text{BFFM}_Z = \frac{\langle \psi | \prod_{l \in C'} \mathcal{Z}_l | \psi \rangle}{\sqrt{\langle \psi | \prod_{l \in C} \mathcal{Z}_l | \psi \rangle}}, \quad (7)$$

where C are closed loops, and C' are open strings corresponding to half the respective closed loops [see inset of Fig. 6]. The off-diagonal BFFM_X is defined similarly but with the elementary \mathcal{X} instead of \mathcal{Z} , and diagnoses the confinement of e anyons. The vanishing of both BFFM order parameters is expected in a quantum spin liquid, and this is indeed observed for the optimal ramp (Fig. 6). Together with the convergence of the TEE to values close to $\gamma = \ln 2$ [Fig. 3(b)], we establish the spin liquid-like signatures near the optimal ramping rate up to the length scale accessible in our numerics.

SUPPLEMENTARY MATERIAL

Numerical methods

In this section, we detail the numerical methods used in the main text. We first describe the implementation of the approximately gauge-symmetric architecture on the ruby lattice. Unlike the case of the toric code ground states studied in Ref. [30], simulating Rydberg-atom dynamics on the ruby lattice is more susceptible to numerical instabilities and error accumulation. To address these challenges, we employ several new techniques, including an auxiliary mean-field ansatz, update-clip regularization, an adaptive sampling transition rule, and ratio estimators for Rényi entropy computation.

Approximately-gauge symmetric neural ansatz

We start by discussing the reduction of the effective Hilbert space due to the Rydberg blockade. As mentioned in the main text, for experimental parameters $R_b = 2.4a$, the strong blockade within each triangle ($V_{ij}/\Omega \sim \mathcal{O}(10^2)$) makes configurations with more than one excitation per triangle energetically costly and therefore strongly suppressed. We therefore restrict the local Hilbert space on each triangle to the four states with at most a single excitation (effective spin-3/2). We encode these 4 possible states by a binary 2-element column:

$$\begin{aligned} \begin{array}{c} \text{triangle with 1 top excitation} \end{array}, \begin{array}{c} \text{triangle with 1 bottom excitation} \end{array} &= \begin{pmatrix} -1 \\ -1 \end{pmatrix} & \begin{array}{c} \text{triangle with 1 top excitation} \end{array}, \begin{array}{c} \text{triangle with 1 top excitation} \end{array} &= \begin{pmatrix} 1 \\ -1 \end{pmatrix} \\ \begin{array}{c} \text{triangle with 1 top excitation} \end{array}, \begin{array}{c} \text{triangle with 1 top excitation} \end{array} &= \begin{pmatrix} -1 \\ 1 \end{pmatrix} & \begin{array}{c} \text{triangle with 1 top excitation} \end{array}, \begin{array}{c} \text{triangle with 1 top excitation} \end{array} &= \begin{pmatrix} 1 \\ 1 \end{pmatrix} \end{aligned} \quad (S1)$$

We emphasize that restricting the local Hilbert space does not preclude two excited atoms within the Rydberg blockade radius if they occupy adjacent triangles. We can further define the \mathbb{Z}_2 parity charge at each vertex by the following

$$\begin{array}{c} \text{vertex with 2 excitations} \end{array} = -1 \quad \begin{array}{c} \text{vertex with 2 excitations} \end{array}, \begin{array}{c} \text{vertex with 2 excitations} \end{array} = 1. \quad (S2)$$

We will construct an approximately-symmetric neural network by constructing a gauge invariant and gauge non-invariant pathway. In each pathway we process features with the convolutional neural networks. To fully take advantage of the translation symmetry of the lattice, we combine the sub-lattice degrees of freedom into super-sites so that the number of sites equals the number of unit cells. As a result, the input dimension is $N_{\text{hex}} \times 4$ where N_{hex} is the number of hexagons or unit cells, for the non-invariant component. Within the gauge-invariant layer we use gauge-invariant product non-linearity for each vertex in Eq. S2 within the first layer to map to the gauge invariant sector [30, 45] which results in an input dimension $N_{\text{hex}} \times 3$ for the invariant path (there are three kagome vertices per each hexagon). Later layers have dimension $N_{\text{hex}} \times d^{(n)}$ where $d^{(n)}$ is the number of features of the n^{th} layers.

Let's denote the convolution in the n -th layer followed by point-wise non-linearity $\sigma(\cdot)$ as

$$\mathbf{u}^{(n)} = \sigma \left(\mathbf{W}^{(n-1)} * \mathbf{u}^{(n-1)} + \mathbf{b}^{(n-1)} \right)$$

where we define the convolution operation $*$ by

$$\left[\mathbf{W}^{(n-1)} * \mathbf{u}^{(n-1)} \right]_{\mathbf{a},i} = \sum_j \sum_{\mathbf{r}} \mathbf{W}^{(n-1)}_{\mathbf{r},ij} \mathbf{u}^{(n-1)}_{\mathbf{a}-\mathbf{r},j} \quad (S3)$$

Here, the variational parameters are contained in the weight \mathbf{W} and bias \mathbf{b} tensors. The first index \mathbf{a} is the 2D vector commensurate with the lattice unit vectors such that $\mathbf{a} = a_1 \mathbf{a}_1 + a_2 \mathbf{a}_2$ and $0 \leq a_1, a_2 \leq l$; and i denotes feature index. The length l thus defines the linear size of the kernel. To ensure coupling between all sites, $l \sim L/N_h$ where L is the linear size of the system and N_h is number of hidden layers. Both the gauge-invariant and non-invariant paths have three hidden layers with $d = 8$ features.

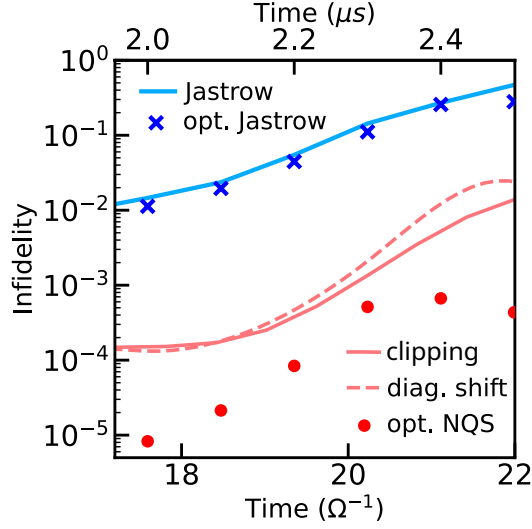


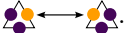
FIG. S1. Infidelity of simulated dynamics compared with exact diagonalization for an $N = 24$ system under the ramping protocol [7]. Lines show TDVP results; points indicate infidelity from direct optimization with the exact ED wavefunction. Blue lines and crosses: decorated Jastrow ansatz (data from [27]). Dashed red line: TDVP with approximately symmetric NQS and diagonal-shift regularization ($\epsilon = 10^{-6}$). Solid red line and dots: TDVP with approximately symmetric NQS using update-clip regularization.

After the last layer of convolution, the outputs from the gauge-invariant (inv) and non-invariant (non-inv) paths are combined element-wise before passing through a non-linear activation function and an average pooling layer to yield a scalar output.

$$\theta^{NN} = \text{AvgPool} \left[\sigma \left(\mathbf{W}^{(N_h-1), \text{inv}} * \mathbf{u}^{(N_h-1), \text{inv}} + \mathbf{W}^{(N_h-1), \text{non-inv}} * \mathbf{u}^{(N_h-1), \text{non-inv}} + \mathbf{b}^{(N_h-1)} \right) \right] \quad (\text{S4})$$

For the first and second hidden layers, we choose the activation function $\sigma(x) = x/2 + x^2/4$ and $\sigma(x) = x/2 + x^2/4 - x^4/48$ for the last layer before output. These choices are Taylor expansions of the swish non-linearity $\sigma(x) = x/(1+e^{-x})$ [55]. We use the Taylor expansion of the non-linear function rather than the actual function to ensure that it is holomorphic with complex inputs. The scalar output of the neural network is obtained by averaging over all elements of the last hidden layers. To include other lattice symmetries such as the C_6 rotation and the $\mathcal{M}_{x,y}$ mirror reflections, we symmetrize the output by

$$\tilde{\theta}^{NN}(s) = \frac{1}{|G|} \sum_{g \in G} \theta^{NN}(gs). \quad (\text{S5})$$

We note that due to the way we encode the physical lattice, a physical transformation not only permutes elements of the inputs but also changes their values. For example, a reflection changes the position of a triangle and additionally exchanges the internal states .

Next, to enhance the stability during the time evolution for dynamics, or optimization for ground state search, we insert a mean-field ansatz beside the symmetrized neural networks [see End Matter of the main text]

$$\log \psi(s) = \theta^{MF}(s) + \tilde{\theta}^{NN}(s). \quad (\text{S6})$$

We note that the mean-field ansatz used here benefits both the ground state optimization and dynamics simulations performed in the main text, especially at early times. Finally, we further test convergence on large systems by confirming that the dynamics of observables is unchanged across several choices of hyperparameters.

Time-evolution and TDVP

We evolve the neural-network state in time using the time-dependent variational principle (TDVP), which governs the evolution of the network parameters $\alpha(t)$. TDVP can be understood as finding a parameter update $(\delta\alpha)^*$ such

that

$$(\delta\alpha)^* = \operatorname{argmin}_{\delta\alpha} \mathcal{D}(|\psi_{\alpha+\delta\alpha}\rangle, e^{-iH\tau} |\psi_{\alpha}\rangle), \quad (\text{S7})$$

where one chooses the quantum state infidelity as a measure of distance,

$$\mathcal{D}(|\phi\rangle, |\psi\rangle) = 1 - \sqrt{\frac{\langle\phi|\psi\rangle\langle\psi|\phi\rangle}{\langle\phi|\phi\rangle\langle\psi|\psi\rangle}}. \quad (\text{S8})$$

One way of arriving at a solution to this equation is by direct minimization of this distance function which can be accomplished e.g., by (natural) gradient descent [56, 57].

Alternatively, when $\delta\alpha = \dot{\alpha}\tau$ and $\tau \ll 1$ we can expand Eq. (S7) up to the second order in $\mathcal{O}(\tau^2)$. The quadratic function can be minimized analytically and gives a closed-form solution for the parameter update equation [33, 58]

$$\sum_k \mathbf{S}_{jk} \dot{\alpha}_k = -i\mathbf{F}_j \quad (\text{S9})$$

where the quantum geometric tensor \mathbf{S} and the force \mathbf{F} are given by

$$\begin{aligned} \mathbf{S}_{jk} &= \frac{\langle\partial_{\alpha_j}\psi|\partial_{\alpha_k}\psi\rangle}{\langle\psi|\psi\rangle} - \frac{\langle\partial_{\alpha_j}\psi|\psi\rangle}{\langle\psi|\psi\rangle} \frac{\langle\psi|\partial_{\alpha_k}\psi\rangle}{\langle\psi|\psi\rangle}, \\ \mathbf{F}_j &= \frac{\langle\partial_{\alpha_j}\psi|H\psi\rangle}{\langle\psi|\psi\rangle} - \frac{\langle\partial_{\alpha_j}\psi|\psi\rangle}{\langle\psi|\psi\rangle} \frac{\langle\psi|H\psi\rangle}{\langle\psi|\psi\rangle}. \end{aligned} \quad (\text{S10})$$

The system of equations (S9) is the core of the TDVP method, which reduces quantum time evolution to iteratively solving a set of coupled ODEs for $\dot{\alpha}$. The resulting one-step update is integrated using the second-order Heun method. We choose the time step $dt = 10^{-2} \Omega^{-1}$.

TDVP regularization

Naively solving the TDVP equation is challenging because S is typically ill-conditioned, making its (pseudo-) inversion numerically unstable. A common remedy is to apply Tikhonov regularization [59], which adds a small constant to the diagonal elements, $S_{ii} \rightarrow S_{ii} + \epsilon$. This shifts all eigenvalues, $\lambda_i \rightarrow \lambda_i + \epsilon$, predominantly affecting the smallest ones and effectively capping the inverse eigenvalues at $1/\epsilon$. However, choosing a large ϵ can distort the trajectory of $\alpha(t)$, deviating it from the true real-time evolution.

A related approach is to apply an eigenvalue cutoff for the S -matrix. It can be understood as follows. Diagonalizing

$$\mathbf{S} = \mathbf{U}\mathbf{\Lambda}\mathbf{U}^\dagger, \quad (\text{S11})$$

where \mathbf{U} is unitary and $\mathbf{\Lambda}$ is a diagonal matrix of singular values, Eq. S9 can be written in the eigenbasis as

$$\tilde{\alpha} = \mathbf{\Lambda}^{-1} \tilde{\mathbf{F}}. \quad (\text{S12})$$

with $\tilde{\alpha} = \mathbf{U}^\dagger \dot{\alpha}$ and $\tilde{\mathbf{F}} = -i\mathbf{U}^\dagger \mathbf{F}$. Within this regularization method, eigenvalues smaller than a chosen threshold, $\lambda < \lambda_{\text{threshold}}$, are discarded.

In this work, we use a different approach: instead of regularizing the singular values λ_k of the matrix S , we focus on $\tilde{\alpha}_k = \tilde{F}_k/\lambda_k$. Specifically, $\tilde{\alpha}_k$ is clipped at μ_k by

$$\tilde{\alpha}_k \rightarrow \begin{cases} \tilde{\alpha}_k, & |\tilde{\alpha}_k| \leq \mu_k, \\ \mu_k \frac{\tilde{\alpha}_k}{|\tilde{\alpha}_k|}, & |\tilde{\alpha}_k| > \mu_k. \end{cases} \quad (\text{S13})$$

where we define

$$\mu_k = \begin{cases} +\infty & \text{if } \lambda_k / \max_k(\lambda) > 10^{-5} \\ 0.5 & \text{if } 10^{-5} \geq \lambda_k / \max_k(\lambda) > 10^{-8} \\ 0.01 & \text{otherwise} \end{cases}. \quad (\text{S14})$$

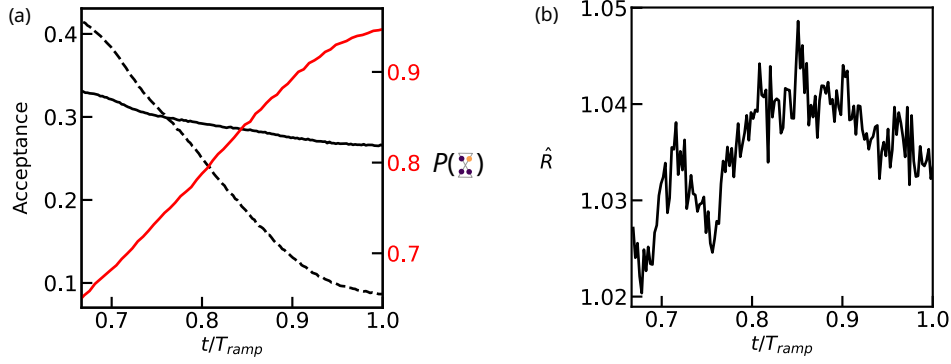


FIG. S2. (a) Markov-chain acceptance rate with plaquette-flip probability $p = 0.1$ (dashed) and $p = 0.4$ (solid). The red line shows the projection of the state onto the Gauss-law fulfilling manifold. Single-spin flips yield lower acceptance when the state converges to a small sector within the Hilbert space. (b) Split-Rhat diagnosis \hat{R} from Hamiltonian evaluation during the ramp. Good simulations have \hat{R} values less than 1.1 [60].

Compared to diagonal-shift regularization, which constrains the *overall* magnitude of the update vector $\sum_j |\tilde{\alpha}_j|^2$, our approach imposes *individual bounds* on each coordinate. This per-coordinate clipping directly suppresses excessively large components $\tilde{\alpha}_k$ that typically arise from small singular values λ_k in the quantum geometric tensor. By selectively damping these ill-conditioned directions, our method allocates the numerical error budget more efficiently. From the perspective of eigenvalue regularization, it can be viewed as a softer variant that lowers the noise floor by removing the most destabilizing components.

To evaluate the effectiveness of our regularization strategy, we compare the per-coordinate constraint with the conventional diagonal shift (global constraint). As shown in Fig. S1, our approach reduces the final-state error by roughly a factor of two, and this improvement remains robust to small variations in the regularization parameters in Eq. S14. For highly expressive NQS architectures, directly optimizing the overlap with the exact wavefunction achieves significantly higher accuracy than TDVP-based evolution, underscoring the importance of maintaining numerical stability during time evolution (and consequently of the regularization method). In contrast, for the more restricted decorated Jastrow ansatz [27], the TDVP results already reach the accuracy limit set by direct optimization, rendering further fine-tuning unnecessary.

Sampling and Markov Chain Monte Carlo statistics

We now describe the calculation of observables within the NQS ansatz, evaluated using Markov chain Monte Carlo sampling. Multiple Markov chains of bit-string configurations, $s_0 \rightarrow s_1 \rightarrow \dots$, are generated via the Metropolis–Hastings algorithm with a chosen update rule. The standard NQS update involves single-spin flips; however, at late ramp times, when Gauss laws emerge, this approach leads to low acceptance rates and poor ergodicity (see Fig. S2). To improve sampling, we adopt a hybrid update scheme combining single-spin and plaquette flips. The plaquette flips, analogous to the action of \mathcal{X}_6 , preserve the Gauss laws. During each Markov step, a plaquette flip is chosen with probability p and a single-spin flip with probability $1 - p$. Convergence across chains is monitored using the split- \hat{R} diagnostic, with $\hat{R} < 1.1$ indicating good convergence. Setting $p = 0.4$ near the end of the ramp yields an acceptance rate above 20% while maintaining $\hat{R} < 1.05$.

Rényi–2 entropy computation

Next, we discuss how to evaluate the entanglement entropy within variational Monte Carlo. The entanglement entropy is non-linear in the density matrix, but can be accessed by measuring expectation value on two copies

$$S_A = -\ln \text{Tr}(\rho_A^2) = -\ln \text{Tr}[(\rho \otimes \rho) \text{SWAP}_A], \quad (\text{S15})$$

where $\rho_A = \text{Tr}_{\bar{A}} \rho$ is the reduced density matrix obtained by tracing out the complementary partition \bar{A} , $\rho \otimes \rho$ is built from stacking two copies of the state ρ and SWAP_A is the operator swapping all sites within subsystem A between

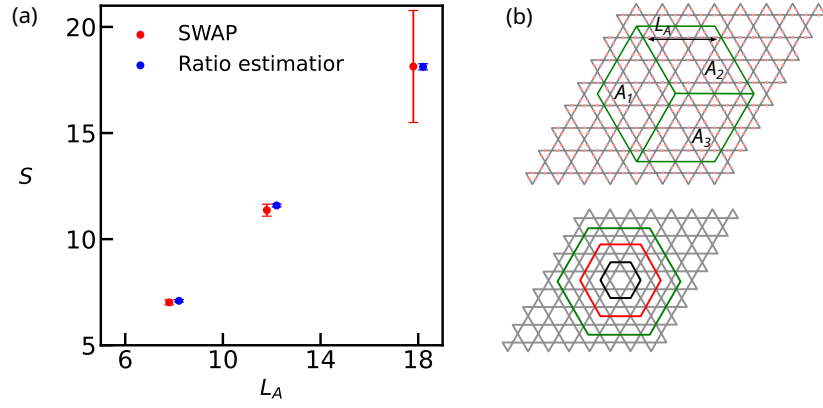


FIG. S3. (a) Rényi entropy with respect the subsystem boundary lengths evaluated by the naive implementation of SWAP operator (red) and the sequential ratio estimators (blue) at the end of the ramp of $\Gamma = 0.096 \Omega$. The ratio estimators use 48 intermediate points between $t = 0.8 T_{ramp}$ and $t = T_{ramp}$, the number of samples $N_s = 294912$ in both cases. (b) Top: Division of a subsystem (the largest hexagon) into three adjacent partitions for the computation of TEE according to Eq. (S22). The depicted subsystem has linear size $L_A = 6$. Bottom: Subsystem sizes to study the scaling of TEE. The colors correspond to Fig. 3(b) of the main text with $L_A = 2, 4, 6$ from the smallest to largest.

the two copies. Eq. (S15) provides a route to evaluate S by sampling over the doubled Hilbert space. A basis element x of the doubled Hilbert space refers to the concatenation (σ, η) of two basis vectors in the original Hilbert space. For conciseness, we denote the integrand of the SWAP action as

$$F(x; A, \psi) = \psi(\eta_A, \eta_{\bar{A}}) \psi(\sigma_A, \sigma_{\bar{A}}) \psi^*(\eta_A, \sigma_{\bar{A}}) \psi^*(\sigma_A, \eta_{\bar{A}}). \quad (\text{S16})$$

Analogously, $F(x; \emptyset, \psi) = |\psi(\sigma)|^2 |\psi(\eta)|^2$ and

$$S_A = -\log \left[\frac{\sum_x F(x; A, \psi)}{\sum_x F(x; \emptyset, \psi)} \right] = -\log \left[\mathbb{E}_{x \sim \mathbb{P}(x)} \frac{F(x; A, \psi)}{F(x; \emptyset, \psi)} \right]. \quad (\text{S17})$$

where $\mathbb{P}(x) = F(x; \emptyset, \psi) / \sum_x F(x; \emptyset, \psi)$ is the distribution in the double Hilbert space. Since we do Markov chain Monte Carlo sampling, we draw samples from the unnormalized $F(x; \emptyset, \psi)$.

In general, the entanglement entropy scales with either the boundary or the volume of the subsystem, making $\langle \text{SWAP} \rangle$ exponentially small in system size and thus requiring often an impractically large number of samples. To overcome the sampling issue, Ref. [61] proposed the “ratio estimator” route by computing the entropy increment along a path. Specifically,

$$S_{A_N} = (S_{A_N} - S_{A_{N-1}}) + (S_{A_{N-1}} - S_{A_{N-2}}) + \cdots + (S_{A_1} - S_{A_0}) + S_{A_0} = S_{A_0} + \sum_n \Delta S_n \quad (\text{S18})$$

where $\{A_0, A_1, \dots, A_N\}$ is a sequence of larger partitions from the smallest A_0 to the target partition A_N . Since entropy scales with the subsystem size, one can, in principle, choose a sequence such that $\Delta S_n \approx \text{const}$. Then, by evaluating the individual ΔS_n and summing them up, one can shift the exponential cost e^S to a linear cost, $(S/\Delta S)e^{\Delta S}$. The key advantage is that one can evaluate ΔS directly by reweighting sampling. The entropy difference, e.g. $\Delta S = S_{A_1} - S_{A_0}$ is estimated by

$$\Delta S = -\log \left[\frac{\sum_x F(x; A_1, \psi)}{\sum_x F(x; A_0, \psi)} \right] = -\log \left[\mathbb{E}_{x \sim F(x; A_0, \psi)} \frac{F(x; A_1, \psi)}{F(x; A_0, \psi)} \right]. \quad (\text{S19})$$

We note that $F(x; A_0, \psi)$ has to be non-negative to become a valid distribution. This can be satisfied automatically if ψ is real and non-negative.

To adapt this idea to our case we note (i) the wavefunction is complex and (ii) the path we use to compute entropy increment is controlled by the evolution time instead of scaling partition size. To tackle complex wavefunctions, we first distinguish the amplitude and phase, $\psi(\sigma) = \Psi(\sigma)e^{i\theta(\sigma)}$. Then the total entropy $S = S^{\text{Am}} + S^{\text{Ph}}$, where

$$S^{\text{Am}} = -\log \left[\frac{\sum_x F(x; A, \Psi)}{\sum_x F(x; \emptyset, \Psi)} \right], \quad S^{\text{Ph}} = -\log \left[\frac{\sum_x F(x; A, \psi)}{\sum_x F(x; A, \Psi)} \right]. \quad (\text{S20})$$

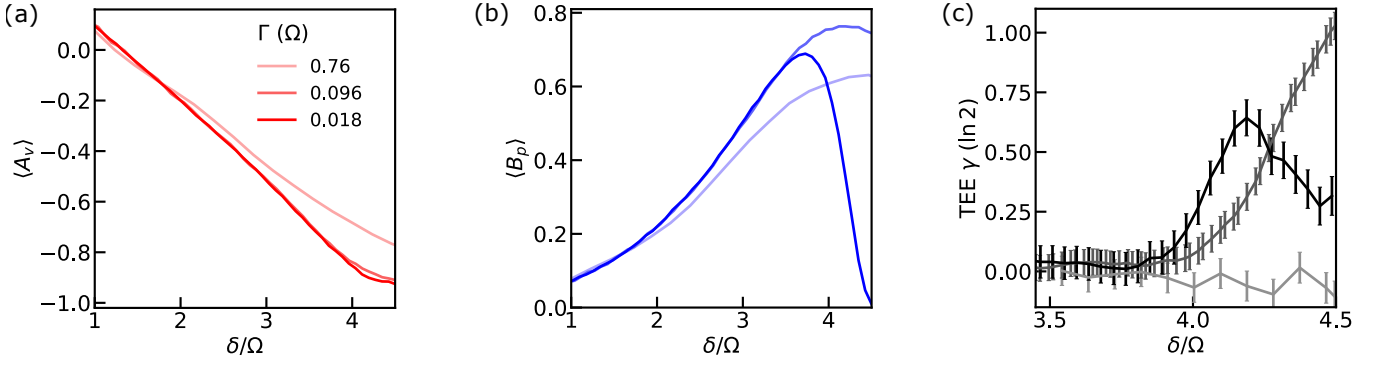


FIG. S4. Dynamic preparation under the diabatic, semi-adiabatic, and adiabatic ramps (from the lightest to boldest colors), tracking various observables: (a) Gauss law, (b) resonance, (c) topological entanglement entropy for $L_A = 6$.

By construction $F(x; A, \Psi)$ is non-negative as Ψ is non-negative, so S^{Ph} can be evaluated using the same framework as Eq. (S19). Under a slow ramp, the state stays close to a ground state that is nonnegative, so S^{Ph} is usually small, and does not suffer from the exponential complexity. For the TEE shown in the main text, we include both S^{Am} and S^{Ph} .

The extensiveness of entropy is mostly contained in S^{Am} , which can be handled by sufficient ratio estimators of intermediate steps. The dynamics of interest starts with a product state with small entanglement entropy that can be efficiently evaluated by the usual naive method. Additionally, the entropy increment from one instant to another can be made arbitrarily small by tuning the time step, allowing us to evaluate the entanglement entropy and topological entanglement entropy to a high resolution. Specifically, $\Delta S_t = S_t^{\text{Am}} - S_{t-\tau}^{\text{Am}}$ can be evaluated via

$$\Delta S_t = -\log \left[\frac{\sum_x F(x; A, \Psi_t)}{\sum_x F(x; A, \Psi_{t-\tau})} \right] + \log \left[\frac{\sum_x F(x; \emptyset, \Psi_t)}{\sum_x F(x; \emptyset, \Psi_{t-\tau})} \right]. \quad (\text{S21})$$

Compared to Eq. (S19), Eq. (S21) contains two terms, but the extra term does not depend on the subsystem and can be reused for other subsystems.

To obtain the topological entanglement entropy over a subsystem $A = A_1 \cup A_2 \cup A_3$ [see Fig. S3(b)], we use the Kitaev-Preskill formula [2]

$$-\gamma = S_{A_1} + S_{A_2} + S_{A_3} - S_{A_1 A_2} - S_{A_2 A_3} - S_{A_1 A_3} + S_{A_1 A_2 A_3}. \quad (\text{S22})$$

By scaling the size of A , we reveal the finite-size characteristics of the dynamically prepared QSL.

Additional numerical data

In Fig. S4, we complement Fig. 2(a) in the main text by comparing the behavior at different ramp rates. Into the VBS phase $\delta/\Omega = 4.5$, the Gauss' law $\langle A_v \rangle$ improves consistently with slower ramps [Fig. S4(a)]. In contrast, the resonance $\langle B_p \rangle$ exhibits a peak at an intermediate rate, but vanishes when the ramp is closer to the adiabatic limit [Fig. S4(b)]. The difference among diabatic, semi-adiabatic, and adiabatic ramps are more pronounced in more global properties such as the topological entanglement entropy as shown in Fig. S4(c). For a fast ramp, the TEE (for $L_A = 6$) stays around zero regardless of the detuning, showing that the state at any points remains trivial. At the slow-ramp limit, the state at large δ also shows with vanishing TEE. However, unlike the fast-ramp limit where the zero TEE is the remnant from the initial trivial state, adiabatically prepared state is close to the VBS ground state of the instantaneous Hamiltonian. This is apparent from a peak of TEE during the sweep, indicating a phase crossover. Therefore, only for intermediate values of the ramping rate does the TEE approach $\ln 2$ as the detuning is swept into the VBS phase.

In Fig. S5, we provide additional data for extracting the two length scale λ and ξ in the main text. The raw data of the Wilson \mathcal{Z} loop is shown in Fig. S5(a) with respect to the loop perimeter. The data shows a deviation from a linear relation at large loops. Indeed, the normalized measured of the Wilson loop $W_A^{\mathcal{Z}}/W_A^{\mathcal{Z},f}$ exhibits a pure area-law decay, from which we extract the length scale λ .

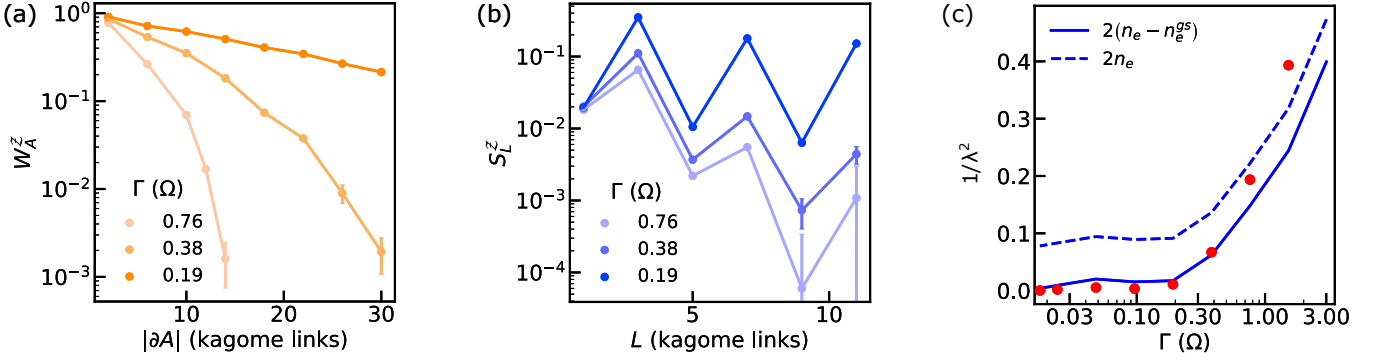


FIG. S5. (a) Scaling of the closed Z loop with respect to the loop perimeter. (b) Amplitude of open Z string with respect to the string length. With sufficiently slow ramp, the open strings show a prominent solid order. (c) The decaying coefficient of the closed Z loop $1/\lambda^2$ with respect to the area (dots) superimposed with the free e anyon density (solid line).

The length scale ξ used in the main text is extracted from scaling of the open Z strings with the fitting ansatz.

$$\langle S_L^Z \rangle \sim e^{-L/\xi} \times \begin{cases} A_1 & \text{if } L-1 \pmod{4} \equiv 0 \\ A_2 & \text{otherwise} \end{cases}. \quad (\text{S23})$$

The two coefficients A_1 and A_2 originate from the symmetry breaking pattern in the VBS phase where the ground state unit cell is doubled compared to the ruby lattice unit cell. The data is shown in Fig. S5(b). This length scale can be related to the perimeter-law decay of the Wilson \mathcal{X} loops. $W_A^{\mathcal{X}}$ measures the parity of Z -strings crossing the boundary ∂A , thus $W_A^{\mathcal{X}} \propto e^{-n_m \xi |\partial A|}$. Figure S5(c) supports our dilute free e gas argument described in the main text by showing that $1/\lambda^2 \approx 2(n_e - n_e^{gs})$ at different ramp rates.

Even though the area-law scaling of the Wilson Z loops is well justified within our numerics, it is supposedly unstable in terms of general gauge theory, i.e. the area-law scaling only exists in the finely tuned gauge-free case [62]. We now provide a simplified model justifying this scaling relation. We digress from the physical state on the ruby lattice and consider a toric-code-like state where the e (m)-condensate is identified with $|+\rangle^{\otimes N}$ ($|\uparrow\rangle^{\otimes N}$). At large length scale, the state is connected to an e condensate, so we can write an effective description for the state as

$$|\psi\rangle = P(\alpha A_v, \beta Z_i) |+\rangle^{\otimes N}, \quad (\text{S24})$$

where P is a general (potentially infinite order) polynomial of the elementary Z -loop operators A_v with characteristic strength α and on-site Z_i with strength β . Upon expanding the Z -Wilson loop $\langle \psi | W_A^Z | \psi \rangle$, only terms where W_A^Z is canceled out by Z operators contained in $|\psi\rangle$ have non-zero contribution, giving

$$\langle \psi | W_A^Z | \psi \rangle = C_1(\alpha)^{|A|} + \dots + C_2(\beta)^{|\partial A|}. \quad (\text{S25})$$

The first term, corresponding to $W_A^Z = \prod_{v \in A} A_v$, gives an area-law decay. Alternatively, $W_A^Z = \prod_{i \in \partial A} Z_i$, producing another perimeter-law component. As apparent in Eqn. (S25), the perimeter law will eventually dominate in the $A \rightarrow \infty$ limit. However, our numerical results exhibit an area-law without any crossover at accessible length scale, suggesting the effective $\alpha \gg \beta$. To verify this assumption, we shift to the open Z -string operators. Within the same perturbative framework as for the Z -loops,

$$\langle \psi | S_L^Z | \psi \rangle \propto \beta^L + \dots \quad (\text{S26})$$

The leading term is given in β only because any products of A_v produce closed loops. Using the same definition of two length scales λ and ξ , we can identify $\lambda = 1/\sqrt{-\ln \alpha}$ and $\xi = 1/(-\ln \beta)$. From Eqn. (S25), the crossover length scale from the area to perimeter-law at long length scale is given by

$$L_{\text{crossover}} = \frac{\ln \beta}{\ln \alpha} = \frac{\lambda^2}{\xi} \quad (\text{S27})$$

As shown in Fig. 4(d), for sufficiently large Γ , $L_{\text{crossover}}$ far exceeds the accessible length scale, self-consistent with the assumption $\alpha \gg \beta$. Intuitively, in our ruby lattice model, the strength α associated with A_v relates to the blockade interaction, while β —given by high-order perturbative process or the long-range tail of the interaction—is usually much weaker.